

Multi-Static UWB Radar-based Passive Human Tracking Using COTS Devices

Chenglong Li, Emmeric Tanghe, *Member, IEEE*, Jaron Fontaine, Luc Martens, *Member, IEEE*,
Jac Romme, Gaurav Singh, Eli De Poorter, and Wout Joseph, *Senior Member, IEEE*

Abstract—Due to its high delay resolution, the ultra-wideband (UWB) technique has been widely adopted for fine-grained indoor localization. Instead of active positioning, multi-static UWB radar-based passive human tracking is explored using commercial off-the-shelf (COTS) devices. To extract the time-of-flight (ToF) reflected by the moving person, channel impulse responses (CIR) and the corresponding variances are used to train the convolutional neural networks (CNN) model. Particle filter algorithm is adopted to track the moving person based on the extracted ToFs of all pairs of links. Experimental results show that the proposed CIR- and variance-based CNN models achieve 30.12-cm and 29.04-cm root-mean-square errors (RMSEs), respectively. Especially, the variance-based CNN model is robust to the scenario changing and promising for practical applications.

Index Terms—Indoor localization, Internet-of-Things (IoT), passive tracking, ultra-wideband (UWB), channel impulse response (CIR), deep learning.

I. INTRODUCTION

LOCATION awareness is an essential feature of the extensive applications in Internet-of-things (IoT), such as location-based services, security monitoring, elderly care, etc. Especially, radio frequency (RF)-based passive sensing (or tracking) has attracted increasing attention recently due to avoiding devices attached to the users. This is appreciated in specific use cases, such as customer behavior analysis and intruder detection. Moreover, compared with the conventional vision-based methods, RF-based passive sensing is little affected by the poor visibility and has no privacy issue, which is desirable for practical use. Passive sensing is reminiscent of the radar systems firstly invented in the early 20th century. But as hardware advancement, it is also possible for the lower-power commercial devices, for example wireless fidelity (WiFi) [1]–[3], millimeter-wave radios [4], [5], and ultra-wideband (UWB) [6], [7], to enable the abundant applications in the field of smart IoT. Given the widespread applications of WiFi, many recent innovations on passive sensing are based on WiFi signals, especially after the physical layer information (namely channel response) is available on commodity WiFi

devices [8], [9]. But the positioning accuracy of WiFi is restricted to meter level (or sub-meter level) generally resulting from the bandwidth limitation.

UWB has been widely adopted in RF devices for the past five years, e.g., smartphones and car keys, which spawns extensive research on UWB-based applications. [10] proposed the UWB-based human breathing motion tracking. The direct background subtraction method was adopted to mitigate the background CIR from the dynamic CIR. The prototype was implemented in an anechoic chamber and achieved centimeter-level accuracy. In [11], UWB radar was introduced for the through-the-wall human detection, which could be used for life signal identification after a catastrophe. In [12], UWB-based human passive tracking was investigated. Based on Kullback-Leibler divergence, [12] proposed to estimate the reflected ToF through quantifying the power change between background and dynamic CIRs. Moreover, UWB passive sensing has also been applied for crowd counting [13] and remote health monitoring [14] very recently, which are significant, especially in the case of social distancing during the pandemic. However, most UWB passive sensing applications are based on the vector network analyzer (VNA) or other dedicated setups with perfect system settings (e.g., very accurate synchronization, high sampling rate, etc.). Instead of the dedicated devices, [7], [15] adopted the low-cost and commercial off-the-shelf (COTS) UWB modules for passive human monitoring and tracking and achieved promising results.

This paper focuses on fine-grained passive human tracking based on COTS UWB devices (Decawave DW1000 [16]). Experimental analysis shows that the accumulated CIRs in case of a person moving have more distinct fluctuations than the static scenario where nobody moves. Taking advantage of this observation, we have proposed two ToF (reflected by the body) estimation methods based on the CIR- and variance-based convolutional neural networks (CNN) models. The remainder of this paper is organized as follows. In Section II, the UWB radar experimental campaign is introduced. CIR preprocessing, the reflected ToF estimation, and particle filter-based human tracking are presented in Section III. The performance evaluation is given in Section IV. Section V concludes this paper.

II. UWB RADAR EXPERIMENT

In this section, the multi-static UWB radar-based human passive tracking experiment will be introduced. The corresponding UWB dataset for passive human tracking is open-access [17]. The explanation of the dataset will be briefly

This work is supported in part by the Excellence of Science (EOS) project MUlti-SERvice Wireless NETworks (MUSE-WINET), by the Research Foundation Flanders (FWO) SB Ph.D. fellowship under Grant 1SB7619N, and by the imec co-financed project UWB-IR AAA.

C. Li, E. Tanghe, L. Martens, and W. Joseph are with the WAVES group, Department of Information Technology, Ghent University-imec, 9052 Ghent, Belgium (e-mail: chenglong.li@ugent.be).

J. Romme and G. Singh are with imec-Netherlands, 5656 AE Eindhoven, The Netherlands.

J. Fontaine and E. De Poorter are with the IDLab group, Department of Information Technology, Ghent University-imec, 9052 Ghent, Belgium.

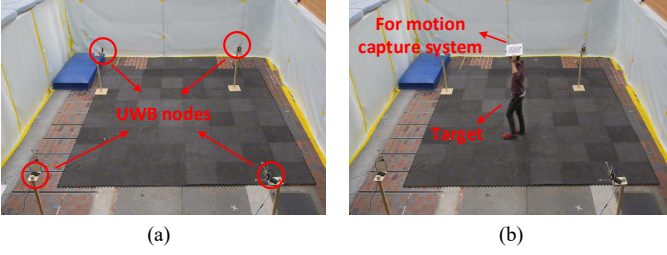


Fig. 1. Measurement campaign of the multi-static UWB radar-based passive human tracking [17]: (a) Background scenario. (b) Dynamic scenario.

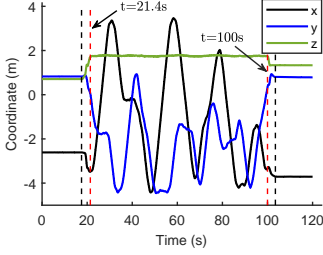


Fig. 2. The ground truth of the marker from the MoCap system.

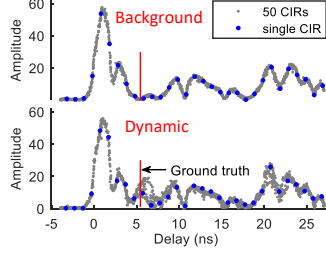


Fig. 3. Amplitude of CIR for background and dynamic scenario.

introduced below. The details can be found in [7], [17]. The ToF reflected by the human body should be estimated based on the collected CIRs to track the moving person. If we have the reflected ToFs of multiple UWB transceivers, the locations of the moving person can be determined via the intersection of the multiple ellipse curves. The UWB passive tracking experiment was conducted in an indoor environment as shown in Fig. 1. The measurement scenarios without and with a single moving person (i.e., background and dynamic scenarios) are shown in Figs. 1 (a) and (b), respectively. The marker on the top of the person's head in Fig. 1(b) was used to obtain the ground truth of the moving trajectory based on the motion capture (MoCap) system. Four UWB nodes with DWM1000 modules were deployed within the targeted area and sent messages to each other with an average frequency of 188 Hz. The pulse repetition frequency is 16 MHz, carrier frequency 3993.6 MHz, and bandwidth 900 MHz. The chipping frequency of DWM1000 is 499.2 MHz, so the time resolution of each CIR sample is 1.0016 ns. The total measurement duration was about two minutes, of which the first 17s and the last 16s indicating the case of no person moving, as shown in Fig. 2. But at the beginning and end of the dynamic measurement, the target's ground truth measured by the MoCap system is not stable. So in this paper, we denote the period between 21.4 s and 100 s as the dynamic scenario for the hereinafter analysis.

III. PASSIVE HUMAN TRACKING MODEL

A. CIR Preprocessing

In the dataset, for each single CIR measurement, only 31 samples have been reported, of which the fourth sample is the first peak (line-of-sight link) identified by DWM1000 using the leading edge algorithm [16]. As mentioned above, the sampling interval of DWM1000 is about one nanosecond, namely about 30 cm in the spatial domain, which is not

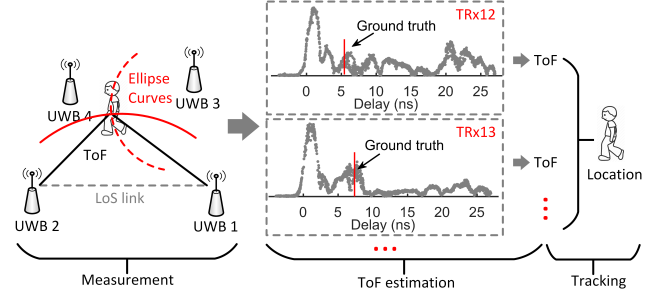


Fig. 4. Multistatic UWB radar-based passive human tracking.

enough to capture the fine-grained spatial variation. To solve this problem, the CIR accumulation technique was proposed in [15]. Specifically, DWM1000 modules were triggered by their local RF clocks in the experiment, and the CIRs between any two UWB nodes were sampled at slightly different times. We can accumulate the CIRs within a short duration and align the CIRs around the reported first peaks. The short duration is set as a sliding window of 50 consecutive CIR measurements. The stride of the sliding window is set as one in this paper. In this way, we can obtain an uneven and oversampled CIR, as shown by the gray dots in Fig. 3, while the blue dots show the amplitude of CIR of a single measurement. The CIR measurements without/with a moving person (background/dynamic) are shown in Fig. 3. The delay (x axis) denotes the ToF difference between the ToF reflected by the moving person and the ToF of the transceiver. Note that we use CIR to represent the amplitude of CIR hereinafter in case of no specific notation.

B. ToF Estimation

For the multi-static UWB radar-based passive human tracking in Fig. 4, the reflected ToFs should be estimated from the collected CIRs. If we obtain the ToFs of the multiple transceivers (TRx) pairs, we can calculate the person's location based on the intersection of the multiple ellipse curves. Specifically, to obtain the reflected ToFs from the CIRs, it is necessary to mitigate the impact of the static LoS component and multipath components (MPCs) from the surroundings. An intuitive idea is the background subtraction adopted in [10]. However, this method is not effective in multipath scenarios [12]. Moreover, the CIRs are aligned based on the reported first peak from the DWM1000 module in the dataset. So the accuracy of the leading edge algorithm in the DWM1000 module also has an impact on the CIRs' subtraction. To this end, the conventional background subtraction method is not suitable for the COTS UWB devices (such as Decawave DM1000).

Fig. 3 shows that the moving person will cause a clear CIR peak around the ground truth (the red vertical line) compared to the background CIR. But according to the experimental results, this is only possible when the person is relatively close to the TRx link. If the reflected path by the moving person is much longer than the LoS length, the signal strength is weak and even much weaker than the MPCs of the surroundings. So it is difficult to distinguish the component of the human

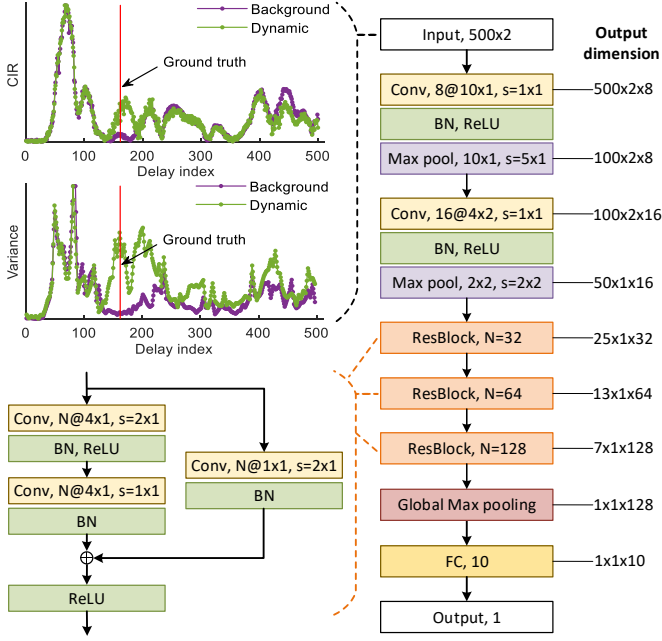


Fig. 5. The designed CNN architecture for ToF estimation.

reflection merely based on the CIR's amplitude. Fortunately, we observe that the moving person causes distinct CIR fluctuations around the ground truth and the following CIR segments with larger delays, as shown in Fig. 3. This phenomenon had also been observed in [7], [15]. Taking advantage of this observation, we propose to pinpoint the reflected ToF on CIR profiles based on CNN. The details are given as follows.

1) *Input of CNN*: After performing the accumulation technique in Section III-A, we can obtain the oversampled CIR with a much higher resolution. When implementing the CNN, we model the reflected ToF estimation as a regression problem. The CNN model will learn the CIR fluctuations and pinpoint where the fluctuations happen on the delay scale. Namely, the output of CNN is the position index where the ground truth is located on the CIR profile. Generally, to speed up the training progress and reduce the parameters of the neural networks, it is necessary to restrict the input size of CNN. On the other hand, the accumulated CIRs have different delay scales between each other. To this end, we resample the CIR linearly along with an even delay scale with, e.g., 500 samples (delay resolution 0.059 ns), and feed the resampled CIRs into the CNN model. The CIR transformation can be given by,

$$\begin{bmatrix} \langle h_{1 \times 31}^{(1)}, \tau_{1 \times 31}^{(1)} \rangle \\ \langle h_{1 \times 31}^{(2)}, \tau_{1 \times 31}^{(2)} \rangle \\ \dots \\ \langle h_{1 \times 31}^{(50)}, \tau_{1 \times 31}^{(50)} \rangle \end{bmatrix} \rightarrow \underbrace{\langle h_{1550 \times 1}, \tau_{1550 \times 1} \rangle}_{\text{sorted}} \rightarrow \underbrace{\langle h_{500 \times 1}, \tau_{500 \times 1} \rangle}_{\text{resampled}}, \quad (1)$$

where h represents the CIR and τ is the corresponding delay of the CIR sampling point.

The moving person will cause the CIR's fluctuations around the ground truth, which has a larger variance than the background CIR. Besides CIRs, the variance of the CIR over a fixed delay interval is another metric that can be used for the reflected ToF estimation. To ensure the effectiveness of

variance, the number of samples within the sliding window along the CIR profile cannot be too small. To this end, we calculate the variance of CIR with a larger interval than the CIR resampling above. For example, the size of the variance series is set as 125 (delay resolution 0.236 ns). In this paper, we want to adopt the same CNN structure for either CIR or variance. So we interpolate the variance to the same size as CIR (i.e., 500) for later training and testing. The variance transformation can be expressed as follows,

$$\langle h_{1550 \times 1}, \tau_{1550 \times 1} \rangle \rightarrow \langle \sigma_{125 \times 1}, \tau_{125 \times 1} \rangle \rightarrow \langle \sigma_{500 \times 1}, \tau_{500 \times 1} \rangle, \quad (2)$$

where σ represents the variance of CIR. An example of the resampled CIR and variance is presented in Fig. 5.

2) *CNN Design*: To estimate the reflected ToF, it is crucial to mitigate the effect of background CIR. Instead of simple background subtraction as in [10], we feed both the background and dynamic metrics (CIRs or variances) into the model and use the CNN to learn the differences between background and dynamic metrics. As mentioned, the output of CNN is the delay index where the ground truth is located on the resampled CIR/variance profile, namely from one to 500. The estimated index can easily be transformed to the reflected ToF by multiplying the resampled series delay resolution. Fig. 5 presents the details of the proposed CNN's architecture. The input is a two-dimensional (2-D) time series data with dynamic and background CIRs/variances. In the designed CNN structure, the elementary convolutional block is adopted: convolution (Conv), batch normalization (BN), activation (ReLU), and pooling layers. The first convolutional block with kernel size 10×1 is designed to perform 1-D convolution, which extracts the features of the input background and dynamic metrics. To reduce the complexity of CNN, a max-pooling layer of 10×1 with stride 5×1 follows. The second convolutional block with kernel size 4×2 is adopted to learn the differences between background and dynamic CIRs/variances. Followed by a global max-pooling layer, three residual blocks (ResBlock) are adopted to further extract the features from the previous layers and avoid the degradation problem of deep networks [18]. Finally, a fully connected (FC) layer outputs the ToF index through the regression layer.

We adopted the Adam optimizer [19] to train the weights of CNN. The batch size is set as 0.05 times of the training set. So it takes 20 iterations to complete one epoch (fully pass the whole training set). The maximum epoch is 100. Early stopping will be triggered to ensure generalization accuracy in case of no validation loss decrease for five epochs. The learning rate is set as 0.001.

C. Particle Filter-based Tracking

After obtaining the reflected ToFs of the multiple pairs of UWB links, we can calculate the possible positions of the moving person. In this section, the particle filter (PF) algorithm [20] is utilized to derive the moving person's trajectory. The state of PF is the 2-D coordinates and velocity of the moving person. A set of K particles has been utilized to estimate the state to represent possible locations within the targeted area. K is set as 200 in this paper. Then the possible target's

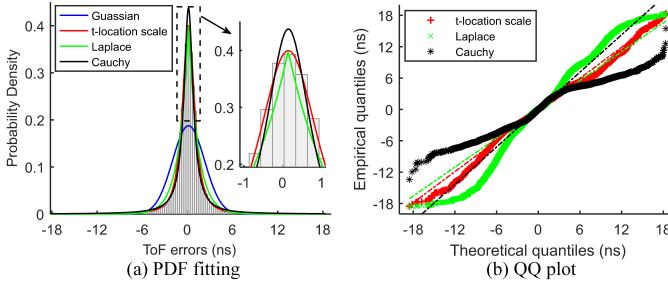


Fig. 6. PDF fitting to the reflected ToFs' errors and the QQ plots.

TABLE I
COMPARISON OF RMSES FOR PASSIVE HUMAN TRACKING IN CM.

	Method in [7]	CIR-based	Variance-based
Case 1	37.53	28.46	26.88
Case 2	34.75	30.12	26.69
Case 3	40.85	28.79	29.04

positions are converted to the reflected ToFs. We update the particles' weights via the probability density function (PDF) of the reflected ToFs' errors. Importance resampling is adopted to obtain N posterior particles and update the target's location.

Importantly, to determine the PDF of the reflected ToFs' errors, we fit the histogram on the validation set with four common distributions (Gaussian, Laplace, Cauchy, and t location-scale distributions). Fig. 6(a) shows the histograms of ToF errors and the PDF fitting results. We can see that Laplace, Cauchy, and t location-scale distributions have much better fitting performance than Gaussian distribution benefiting from the ability to model distributions with heavier tails (outliers). Fig. 6(b) presents the goodness-of-fit of Laplace, Cauchy, and t location-scale distributions via quantile-quantile (QQ) plots. We can observe that the plot (red plus signs) of t location-scale distribution produces an approximately straight line compared to the other two plots, suggesting that the reflected ToFs' errors follow t location-scale distribution in our case.

IV. PERFORMANCE EVALUATION

To validate the tracking accuracy of the proposed CNN-based algorithm, we divide the whole dataset into two parts, namely training and test sets. As mentioned in Section II, the dynamic period with a person moving is from 21.4 s to 100 s, namely 78.6-s duration. We set the duration of the training set as 52.4 s (namely about 66.7% of the whole dataset) and the test set as 26.2 s (33.3%). Fig. 7 shows three cases of dataset partitioning for the algorithm testing. Four UWB nodes (blue triangles in Fig. 7) are adopted in the datasets, so there are six pairs of TRx links. For the training set, we combine the CIR/variance series of all pairs of links. To avoid overfitting, we further partition the training set into two subsets after reshuffling. 85% of the original training set is set as the new training set, and the remaining part is the validation set.

A. Tracking Accuracy

Fig. 8 shows the passive human tracking results based on the proposed CIR- and variance-based CNN methods. We can

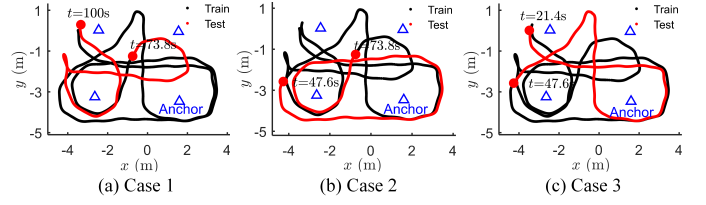


Fig. 7. Training (black) and test (red) sets partitioning on the whole trajectory.

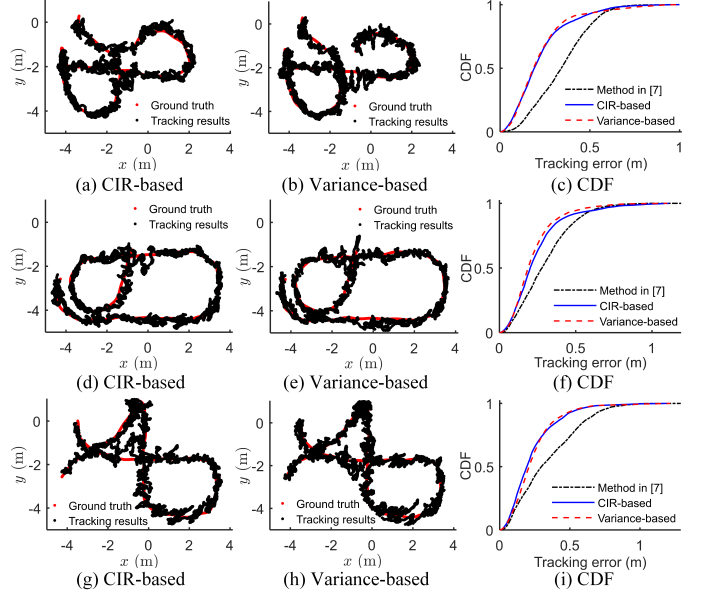


Fig. 8. The passive human tracking accuracy of the proposed CNN methods: (a)-(c) Case 1. (d)-(f) Case 2. (g)-(i) Case 3.

observe from the tracking trajectories that the proposed methods have achieved impressively high positioning accuracy. The accuracy of the CIR- and variance-based CNN models are also compared with the algorithm proposed by [7] which can be regarded as a variance-based leading-edge algorithm. Figs. 8 (c) and (f) present the cumulative distribution function (CDF) of the tracking errors. The proposed CIR- and variance-based CNN models have achieved comparable tracking accuracy with median errors 18.52-20.92 cm and 90-th percentile errors 39.42-46.47 cm. Both of the proposed CIR- and variance-based CNN models outperform the method of [7] with median errors 27.90-34.09 cm and 90-th percentile errors 53.92-66.12 cm. Moreover, the root-mean-square errors (RMSEs) of passive tracking are summarized in Table I. The proposed methods have RMSEs from 26.69 cm to 30.12 cm whereas the algorithm in [7] has achieved 34.75-cm to 40.85-cm RMSEs for the three cases of partitioning.

B. Model Generalization

One of the major drawbacks of the deep learning-based algorithm is the weak generalization ability for different scenarios or datasets. As mentioned, we have combined the CIRs of all pairs of TRx link to train the CNN models. Generally, the CIR (no person moving) of all TRx links are different from each other due to going through different propagation channels and having different interactions (reflections or scattering) with the surroundings. To a great extent, this is similar to the cases

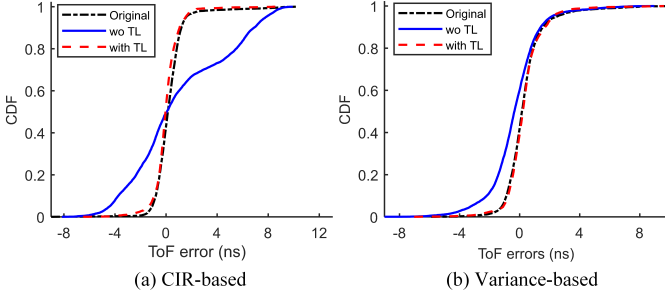


Fig. 9. The reflected ToF estimation accuracy of the proposed CNN methods with and without (wo) transfer learning.

TABLE II
MAES OF THE REFLECTED ToF ESTIMATION ERRORS IN NS.

	Original	without TL	with TL
CIR-based	0.78	3.21	0.69
Variance-based	0.85	1.25	0.82

of the environment/deployment changes. In this section, we will use the different CIR profiles to mimic the environment changing, and investigate the impact of scenario changing on the proposed CNN models.

We utilize the training set without the data from one of the TRx links, labeled as \mathcal{A} , to train the CNN models. The trained models are used to predict the reflected ToF of TRx link \mathcal{A} in the test set. Besides, transfer learning (TL) has been adopted as the benchmark, which replaced the final FC layer and the output layer of the trained models with the new ones. 10 % training set of the TRx link \mathcal{A} has been adopted for TL's retraining. Fig. 9 shows the CDF plots of ToF errors based on CIR and variance models. As shown by the blue line, the estimation accuracy of the CIR-based CNN model without TL is much lower than training using the whole training set of all pairs of links (label as *Original*). In contrast, the variance-based CNN is only slightly affected by the scenario changing as shown in Fig. 9(b). Table II presents the mean absolute errors (MAEs) of the ToF estimation errors. It is clear that the variance-based CNN is more robust to campaign variation (1.25-ns MAEs) compared to the CIR-based CNN model (3.21-ns MAEs), which is promising for practical applications without the need of training from scratch or TL. The experiments in different environments are crucial to further validate the generalization ability of the proposed methods. This is not included in this paper, and we leave it to our future work.

V. CONCLUSION

In this paper, we have proposed a CNN-based passive human tracking method using the COTS UWB devices. The residual CNN models have been designed for both CIR- and variance-based ToF estimation. A particle filter algorithm has been implemented for human tracking. According to experimental validation, the proposed CIR- and variance-based CNN methods have achieved the accuracy of less than 30.12-cm and 29.04-cm RMSEs, respectively. Moreover, the variance-based CNN has better generalization ability and is slightly

environment-dependent than the CIR-based CNN model. The main future works will consist of more experimental evaluation of measurement campaign variation and multi-person passive tracking.

REFERENCES

- [1] X. Li, S. Li, D. Zhang, J. Xiong, Y. Wang, and H. Mei, "Dynamic-MUSIC: Accurate device-free indoor localization," in *Proceedings of the 2016 ACM International Joint Conference on Pervasive and Ubiquitous Computing (UbiComp)*, Sep 2016, p. 196–207.
- [2] Y. Xie, J. Xiong, M. Li, and K. Jamieson, "MD-Track: Leveraging multi-dimensionality for passive indoor Wi-Fi tracking," in *The 25th Annual International Conference on Mobile Computing and Networking (MobiCom)*, Aug 2019, pp. 1–16.
- [3] Q. Gao, J. Tong, J. Wang, Z. Ran, and M. Pan, "Device-free multi-person respiration monitoring using wifi," *IEEE Transactions on Vehicular Technology*, vol. 69, no. 11, pp. 14 083–14 087, 2020.
- [4] T. Wei and X. Zhang, "MTrack: High-precision passive tracking using millimeter wave radios," in *Proceedings of the 21st Annual International Conference on Mobile Computing and Networking (MobiCom)*, Sep 2015, p. 117–129.
- [5] C. Wu, F. Zhang, B. Wang, and K. J. Ray Liu, "mmTrack: Passive multi-person localization using commodity millimeter wave radio," in *IEEE Conference on Computer Communications (INFOCOM)*, Jul 2020, pp. 2400–2409.
- [6] S. Chang, R. Sharan, M. Wolf, N. Mitsumoto, and J. W. Burdick, "UWB radar-based human target tracking," in *2009 IEEE Radar Conference*, May 2009, pp. 1–6.
- [7] A. Ledergerber and R. D'Andrea, "A multi-static radar network with ultra-wideband radio-equipped devices," *Sensors*, vol. 20, no. 6, pp. 1–20, Mar 2020.
- [8] D. Halperin, W. Hu, A. Sheth, and D. Wetherall, "Predictable 802.11 packet delivery from wireless channel measurements," in *Proceedings of the ACM SIGCOMM 2010 Conference (SIGCOMM)*, Aug 2010, p. 159–170.
- [9] Z. Yang, Z. Zhou, and Y. Liu, "From rssi to csi: Indoor localization via channel response," *ACM Computing Surveys*, vol. 46, no. 2, pp. 1–32, Dec 2013.
- [10] J. Salmi and A. F. Molisch, "Propagation parameter estimation, modeling and measurements for ultrawideband MIMO radar," *IEEE Transactions on Antennas and Propagation*, vol. 59, no. 11, pp. 4257–4267, Nov 2011.
- [11] J. Li, Z. Zeng, J. Sun, and F. Liu, "Through-wall detection of human being's movement by UWB radar," *IEEE Geoscience and Remote Sensing Letters*, vol. 9, no. 6, pp. 1079–1083, Nov 2012.
- [12] M. McCracken and N. Patwari, "Hidden markov estimation of bistatic range from cluttered ultra-wideband impulse responses," *IEEE Transactions on Mobile Computing*, vol. 13, no. 7, pp. 1509–1521, Jul 2014.
- [13] J.-H. Choi, J.-E. Kim, and K.-T. Kim, "People counting using IR-UWB radar sensor in a wide area," *IEEE Internet of Things Journal*, vol. 8, no. 7, pp. 5806–5821, Apr 2021.
- [14] F. Khan, A. Ghaffar, N. Khan, and S. H. Cho, "An overview of signal processing techniques for remote health monitoring using impulse radio UWB transceiver," *Sensors*, vol. 20, no. 9, pp. 1–21, April 2020.
- [15] A. Moschovik, E. Tsvetkov, A. Alekseev, and A. Sikora, "Investigations on passive channel impulse response of ultra wide band signals for monitoring and safety applications," in *2016 3rd International Symposium on Wireless Systems within the Conferences on Intelligent Data Acquisition and Advanced Computing Systems (IDAACS-SWS)*, Sep 2016, pp. 97–104.
- [16] Decawave, "DW1000 User Manual," [Online]. Available: https://www.decawave.com/sites/default/files/resources/dw1000_user_manual_2.11.pdf, 2017.
- [17] A. Ledergerber, "Dataset accompanying paper 'A multi-static radar network with ultra-wideband radio-equipped devices'," [Open access]. Available: <https://doi.org/10.3929/ethz-b-000397625>, Feb 2020.
- [18] K. He, X. Zhang, S. Ren, and J. Sun, "Deep residual learning for image recognition," in *Proceedings of the IEEE Conference on Computer Vision and Pattern Recognition (CVPR)*, June 2016, pp. 770–778.
- [19] D. P. Kingma and J. Ba, "Adam: A method for stochastic optimization," *arXiv:1412.6980*, pp. 1–15, Jan 2017.
- [20] F. Gustafsson, F. Gunnarsson, N. Bergman, U. Forssell, J. Jansson, R. Karlsson, and P.-J. Nordlund, "Particle filters for positioning, navigation, and tracking," *IEEE Transactions on Signal Processing*, vol. 50, no. 2, pp. 425–437, Feb 2002.